Electronic Supplementary Material (ESI) for Soft Matter.
This journal is © The Royal Society of Chemistry 2018

Structure formation in soft nanocolloids: Liquid-drop model

Electronic Supplementary Information

A.-K. Doukas,[1] C. N. Likos,[2] and P. Ziherl[1, 3]

[1] *Jožef Stefan Institute, Jamova 39, SI-1000 Ljubljana, Slovenia*
[2] *Faculty of Physics, University of Vienna, Boltzmanngasse 5, A-1090 Vienna, Austria*
[3] *Faculty of Mathematics and Physics, University of Ljubljana, Jadranska 19, SI-1000 Ljubljana, Slovenia*

(Dated: March 16, 2018)

I. IMPLEMENTATION OF A15 AND σ LATTICE

The A15 lattice is a cubic lattice containing two types of inequivalent lattice sites referred to as interstitial and columnar, respectively, and a total of 8 sites per unit cell. The 2 interstitial sites are located in the vertices of the unit cell and in its center just like in the BCC lattice, whereas the 6 columnar sites lie in pairs on the bisectors of the faces of the unit cell oriented such that these sites form sets of columns running along x, y, and z axis (Fig. S1a). The interstitial sites are 12-coordinated with a single nearest-neighbor distance equal to $\sqrt{5}a/4$, where a is the lattice constant, its Wigner-Seitz cell being an irregular dodecahedron (Fig. S1b). The columnar sites have 2 nearest neighbors at a distance of $a/2$ and 12 next-nearest neighbors at a distance of $\sqrt{5}a/4$), its Wigner-Seitz cell being a decatetrahedron (Fig. S1b).

In our implementation, the deformation energy of the A15 lattice is given by a 1:3 weighted average of the deformation energies of the interstitial and the columnar sites computed separately by confining the liquid drop in a dodecahedral and a decatetrahedral cell, respectively. This is numerically much more convenient than considering the whole unit cell with 8 drops at a time. In turn, a separate analysis of the two inequivalent sites requires some care because the true drop-drop contacts are mediated by confinement to the Wigner-Seitz cells, the cell faces serving as an auxiliary device. In single-site lattices such as the SC, FCC, BCC, and SH lattice, mechanical balance of forces on a given contact zone is automatically ensured by symmetry because each contact zone on the reference drop pushes against an identical contact zone on its neighbor. In the A15 lattice the same principle ensures mechanical stability at the large hexagonal faces as well as the pentagonal faces at the contact between two neighboring columnar drops but not at the contacts between the columnar and the interstitial drops.

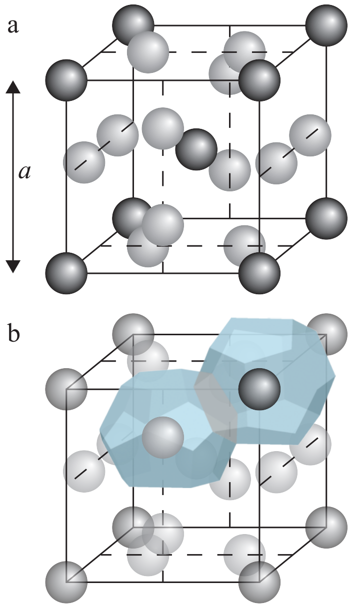

Figure S 1: A15 lattice: the ball-and-stick representation where the interstitial and the columnar sites are represented by black and white spheres, respectively (a), the dodecahedral and the decatetrahedral Wigner-Seitz cells for the interstitial and the columnar sites, respectively (b).

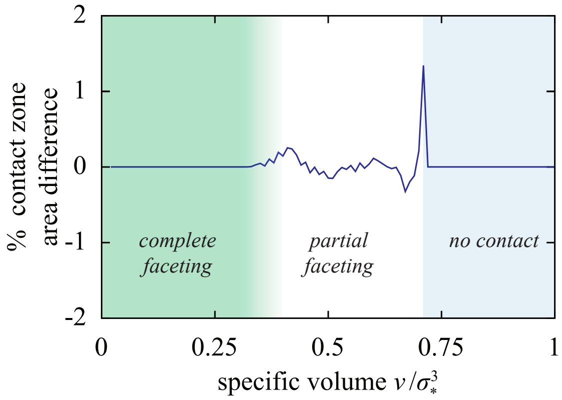

Figure S2: Relative difference of the contact-zone area of a columnar drop that is in contact with an interstitial drop and the contact-zone area of an interstitial drop that is in contact with a columnar drop in the A15 lattice. In the partial-faceting regime, we employ the regular Voronoi tessellation and in the complete-faceting regime we employ the adjusted Voronoi tessellation described below. Also indicated are the complete-faceting, the partial-faceting, and the no-contact regime.

In the partial-faceting regime, the areas of the contact zones of columnar and interstitial drops with the faces of the respective Wigner-Seitz cells are generally slightly different, but as shown in Fig. S2 the relative area difference plotted is less than 0.33% except at a point where the two drops just touch each other; there it reaches about 1.3%. The contribution of this small imbalance of columnar-interstitial contact area to the overall numerical accuracy of our results is marginal.

In the complete-faceting regime, any two neighboring drops must have the same volume so as to ensure that the pressures within the drops are the same. To ensure this, the Voronoi tesselation is modified by displacing the faces of the Wigner-Seitz cells that correspond to the contact between the columnar and the interstitial cells towards the interstitial cell (Fig. S3). Again the displacement needed is small: The two volumes are identical if the the distance between the center of mass of the columnar Wigner-Seitz cell and the columnar-interstitial face is at 50.36% rather than at 50% of the distance betwen the centers of the columnar and the interstitial cells.

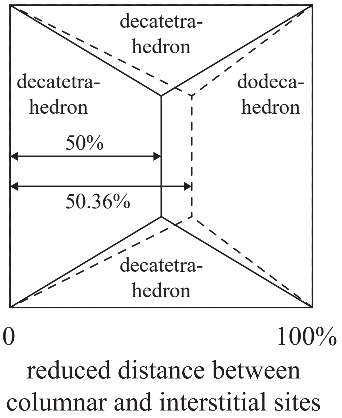

Figure S3: Schematic of the cross-section cutting across the contact zone between 14-coordinated columnar site and 12-coordinated interstitial site. Horizontal axis is the reduced distance from the center of the columnar site expressed in units of center-to-center distance of $\sqrt{5}a/4$. In a Voronoi construction, the contact zone is halfway between the centers (solid lines). To ensure mechanical balance in the complete-faceting regime, the contact zone is slightly displaced towards the center of the interstitial site (dashed lines), the relative displacement amounting to 0.36% of the center-to-center distance.

In the σ lattice, we employ the same algorithm to ensure mechanical balance between drops in the 5 inequivalent lattice sites, and the corrections needed are of the same order of magnitude as in the A15 lattice.

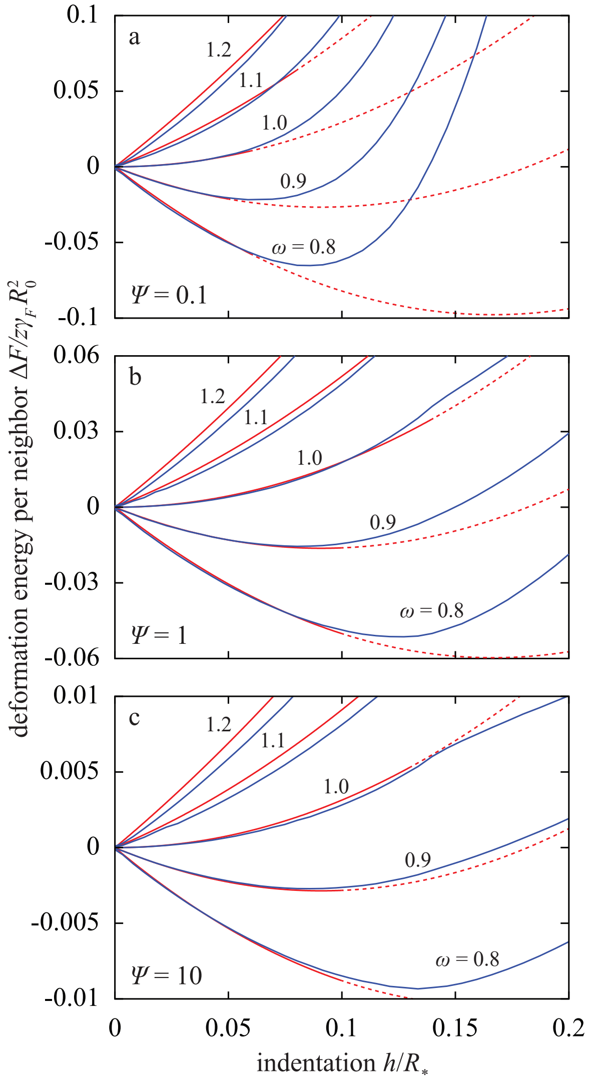

Figure S4: FCC deformation energy per neighbor vs. indentation at $\Psi = 0.1, 1$, and 10 (blue lines in panels a, b, and c, respectively) for ω between 0.8 and 1.2. Red lines in panels a, b, and c are fits based on Eqs. (S12), (S10), and (S13), respectively; in Eq. (S10) we used $R_*/R_0 \approx 0.755$, which corresponds to $\Psi = 1$. Fits are plotted using solid lines at indentations where the deformation energy is pairwise additive.

II. PAIRWISE-ADDITIVE SMALL-DEFORMATION REGIME

Numerical results

Figure 3a of the main text shows the deformation energy per neighbor for $\Psi = 1$ and $\omega = 1$ and 1.1. Here we further elaborate the pairwise-additive regime in the FCC lattice whose low-density version is stable at densities where this regime is relevant. Figures S4a, b, and c show the FCC deformation energy per neighbor for a broader range of ω at $\Psi = 0.1, 1$, and 10, respectively, demonstrating that the linear small-deformation regime is there at all Ψ provided that $\omega \gtrsim 1.1$ or $\lesssim 0.9$. The figure also shows that at $\omega = 1$ the harmonic repulsion is present at all Ψ. Finally, we scanned the small-deformation behavior for ω close to 1 with a step of 0.01 (not shown for clarity) so as to locate the transition between the attractive and the repulsive regime, and we find that is exactly at $\omega = 1$ at all Ψ.

Figure S5 shows the exponent characterizing the small-

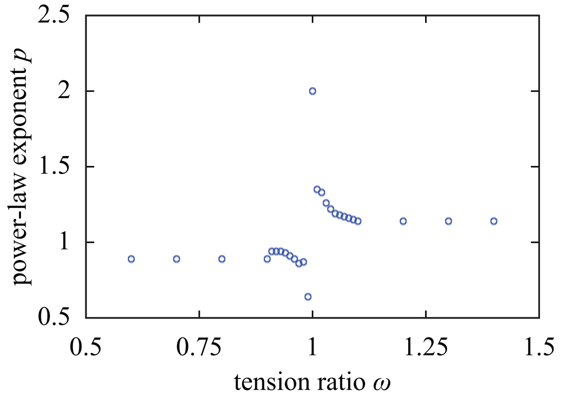

Figure S5: Small-indentation exponent p vs. tension ratio ω between 0.9 and 1.1 for $\Psi = 0.1, 1$, and 10. The $\Psi = 1$ data are plotted using solid circles whereas the $\Psi = 0.1$ and 10 data are plotted using open circles not visible because the three sets of points overlap.

deformation regime in the FCC lattice plotted against tension ratio ω for $\Psi = 0.1, 1$, and 10. This diagram shows that for $\omega \lesssim 0.9$ the power is about 0.89, at $\omega = 1$ it peaks at 2, and at $\omega \gtrsim 1.1$ it levels off at about 1.14.

Theory

The power-law small-deformation regimes can be understood based on geometric arguments, assuming that the part of the drop undergoing indentation is a spherical cap and that the non-contact drop surface is spherical (Fig. S6).

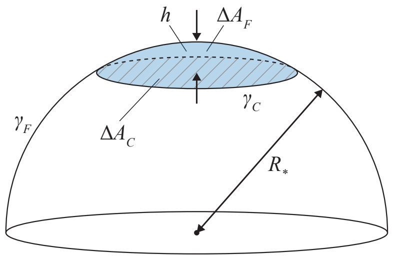

Figure S6: Schematic of the spherical-cap model of indentation of the liquid drop. The decrease of the solvent-drop interfacial area ΔA_F is colored blue whereas the increase of the contact area ΔA_C is hatched.

We first consider the change of surface energy associated with the formation of the contact zone. We disregard any increase of drop radius upon indentation; as shown below, a more detailed analysis shows that such an increase leads to a h^2 term in the deformation energy whereas the leading order term is proportional to h. The change of surface energy due to indentation at a single contact zone is computed by assuming that the drop can be approximated by a truncated sphere, and it depends on the area of the cap before and after indentation. The area of the spherical cap before it undergoes indentation is

$$\Delta A_F = 2\pi R_* h, \tag{S1}$$

where h is indentation. Upon indentation, the cap is flattened and its area reads

$$\Delta A_C = \pi(2R_* - h)h = 2\pi R_* h - \pi h^2. \tag{S2}$$

The total change of surface energy for a single contact zone is $\Delta F_A = \gamma_C \Delta A_C/2 - \gamma_F \Delta A_F$ which is equal to

$$\Delta F_A = 2\pi(\omega - 1)\gamma_F R_* h - \pi\omega\gamma_F h^2. \tag{S3}$$

For small indentations h/R_* and provided that $\omega \neq 1$, this result is dominated by the linear term:

$$\Delta F_A \approx 2\pi(\omega - 1)\gamma_F R_* h, \tag{S4}$$

which explains the numerically obtained almost linear pairwise-additive regime as well as the attractive and the repulsive nature of this interaction at $\omega < 1$ and $\omega > 1$, respectively.

Now we turn to terms proportional to h^2; these do not consist solely of the second term in Eq. (S3), which is negative. Equation (S3) was derived by assuming that the resting radius of the drop does not change, which pertains to very compressible drops with $\Psi \gg 1$. In this case, the bulk energy increases upon indentation because the volume of the drop is decreased by

$$-\Delta V = \pi\left(R_* - \frac{h}{3}\right)h^2 \approx \pi R_* h^2 \tag{S5}$$

for small h/R_*. The corresponding increase of the bulk energy is given by the work expended $W = -p\Delta V$ where $p = 2\gamma_F/R_*$ is the Laplace pressure in the resting drop. Thus

$$\Delta F_{\text{bulk}} = 2\pi\gamma_F h^2. \tag{S6}$$

This means that the total energy change for $\Psi \gg 1$

$$\begin{aligned}\Delta F &= \Delta F_{\text{bulk}} + \Delta F_A\\ &= 2\pi(\omega - 1)\gamma_F R_* h + 2\pi\left(1 - \frac{\omega}{2}\right)\gamma_F h^2,\end{aligned} \tag{S7}$$

showing that for $\omega = 1$, the deformation energy $\propto h^2$. As ω departs from 1, the linear term is increasingly more important at small indentations $h \to 0$. However, the crossover between this regime and that at somewhat larger indentations where the second-order term is comparable to the linear term is evidently proportional to $|\omega - 1|$ and thus small if ω is close to 1. Because of the specific dependence of ΔF on ω, all of Eq. (S7) rather than just its linear part should be regarded as the small-deformation regime.

In the incompressible limit where $\Psi \ll 1$, the volume change on indentation is vanishingly small and the decrease of the drop volume in the cap is compensated by an

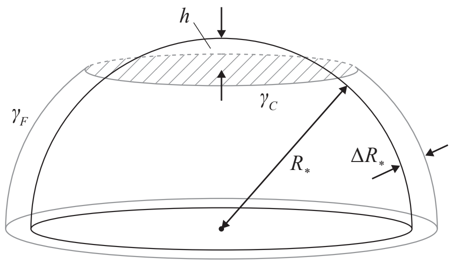

Figure S7: Schematic illustrating the increase of resting radius in incompressible drops.

increase of radius which then leads to an increased surface energy (Fig. S7). To lowest order in h/R_*, the radius increase ΔR_* is determined by $\Delta V = \pi R_* h^2 = 4\pi R^{*2}\Delta R_*$ so that

$$\Delta R_* = \frac{h^2}{4R_*}. \tag{S8}$$

The non-contact area is thus increased by $8\pi R_* \Delta R_* = 2\pi h^2$ and this gives rise to an additional surface term, which needs to be added to Eq. (S3) and reads $2\pi\gamma_F h^2$. Since the bulk energy is constant, the total energy change for $\Psi \ll 1$ thus reads

$$\Delta F = 2\pi(\omega - 1)\gamma_F R_* h + 2\pi\left(1 - \frac{\omega}{2}\right)\gamma_F h^2. \tag{S9}$$

This result is exactly the same as Eq. (S7), which is quite remarkable because the two cases correspond to diametrically opposite extremes, that is to arbitrarily compressible drops with $\Psi \gg 1$ and to incompressible drops with $\Psi \ll 1$.

Using Eq. (S7) or (S9) to interpret the numerically obtained deformation free energy of drops in a given lattice is easiest in lattices with a single type of sites with a single type of neighbors such as the SC, DC, and FCC lattice. In these lattices, the indentations at all drop-drop contacts are identical and thus the total deformation energy at a given density is a sum of z identical terms for each site; here z is the coordination number.

To compare Eqs. (S7) and (S9) with Fig. 3a of the main text and Fig. S4, note that in this paper the deformation energy per contact is expressed in units of $\gamma_F R_0^2$ and that the natural unit of h is R_*, the resting drop radius. Thus we recast these equations, now interpreted as the deformation energy per contact, as

$$\frac{\Delta F}{z\gamma_F R_0^2} = 2\pi\left(\frac{R_*}{R_0}\right)^2\left[(\omega - 1)\frac{h}{R_*} + \left(1 - \frac{\omega}{2}\right)\left(\frac{h}{R_*}\right)^2\right]. \tag{S10}$$

The dimensionless prefactor $(R_*/R_0)^2$ (referred to as λ_Ψ in Ref. [1]) depends on Ψ and is determined by the solution of

$$\left(\frac{R_*}{R_0}\right)^3 + \Psi\left(\frac{R_*}{R_0}\right)^2 - 1 = 0 \tag{S11}$$

[Eq. (5) in Ref. [1]]. This equation can be solved analytically, but it is more illuminating to consider the limiting cases $\Psi \ll 1$ and $\Psi \gg 1$ where $R_*/R_0 \approx 1 - \Psi/3$ and $R_*/R_0 \approx 1/\Psi^{1/2}$, respectively. Thus in reduced units, Eq. (S10) reads

$$\frac{\Delta F}{z\gamma_F R_0^2} = 2\pi\left(1 - \frac{2\Psi}{3}\right) \times \left[(\omega - 1)\frac{h}{R_*} + \left(1 - \frac{\omega}{2}\right)\left(\frac{h}{R_*}\right)^2\right] \tag{S12}$$

for $\Psi \ll 1$ and

$$\frac{\Delta F}{z\gamma_F R_0^2} = \frac{2\pi}{\Psi}\left[(\omega - 1)\frac{h}{R_*} + \left(1 - \frac{\omega}{2}\right)\left(\frac{h}{R_*}\right)^2\right]. \tag{S13}$$

for $\Psi \gg 1$. The fits of the small-deformation pairwise-additive deformation free energy based on Eq. (S10) included in Fig. S4, showing rather good agreement—and suggesting that the numerically found power-law exponents of ≈ 1.14 and 0.89 at $\omega \gtrsim 1.1$ and $\omega \lesssim 0.9$, respectively (Fig. S5), which characterize the drop-drop interaction at small indentations, should be regarded as effective exponents arising from a combination of terms proportional to h and h^2. The data in Fig. S4a and c are fitted using Eq. (S12) and Eq. (S13), respectively, whereas the data in Fig. S4b are fitted using Eq. (S10) with $R_*/R_0 \approx 0.755$, which corresponds to $\Psi = 1$.

In Fig. S4, we plot the fits using solid lines at indentations where the deformation energy is pairwise-additive; the dashed segments extend beyond this regime. This demonstrates that Eqs. (S7) and (S9) and the theory behind them capture the main effects involved although there exists a small systematic residual discrepancy between the slopes at small indentations, especially visible at large Ψ and $\omega > 1$ (such as $\Psi = 10$ and $\omega = 1.2$ in Fig. S4c) where these formulas overestimate the repulsive energy. This discrepancy is not surprising as in our theory the area of the contact zone is calculated by approximating the drop by a truncated sphere whereas in reality this area is determined by the minimum of the total free energy at given indentation. At $\omega > 1$ this minimization leads to a smaller contact zone (and thus a smaller repulsive contact energy) than the geometrical arguments alone, but this is evidently a second-order effect. At the same time, we can think of other refinements of Eqs. (S7) and (S9) to include, e.g., the increase of the contact-zone diameter in drops with $\Psi \ll 1$ due to the increase of the drop radius upon indentation, which is indicated in Fig. 7, or the increase of pressure upon indentation in drops with $\Psi \gg 1$. It is possible that these refinements would further improve the already good agreement.

More importantly, Fig. S4 also shows that Eqs. (S7) and (S9) are valid not only at $\Psi \gg 1$ and $\Psi \ll 1$ where we derived them but also at other values of Ψ as demonstrated by panel b. We are led to conclude that our analytical results for the drop-drop interaction are to a very good approximation universal.

III. NON-CONVEX AND NON-MONOTONIC DEFORMATION ENERGY

The ω-dependent non-convex and non-monotonic deformation energy profiles are not specific to the FCC lattice (Fig. 3b of the main text) but are generally found in all lattices. Figure S8 shows the deformation energies of the FCC, SC, BCC, A15, and σ lattice for the values of $\varPsi$ and ω covered in Fig. 3b of the main text; panel a representing the FCC lattice is replotted from Fig. 3b of the main text for convenience. Qualitatively, the deformation energies of these three lattices are the same as in the FCC lattice in that they too are characterized by i) a hump at a large enough tension ratio ω and a small enough $\varPsi$ and ii) an attraction on contact and a minimum at small enough ω.

The main quantitative differences between the lattices are i) the specific volume where the drops are in contact, which is smallest in the FCC lattice, and ii) the discontinuities of the slope of the deformation energy seen in lattices with more than a single type of neighbors. In the BCC lattice, the second-nearest neighbors touch at $v/\sigma_*^3 \approx 0.49$, which is indicated by an arrow. Also visible are the two slope discontinuities in the A15 lattice (also indicated by arrows) whereas in the σ lattice there are 6 of them, and they are less prominent.

In Fig. S8 as well as in Fig. 3b of the main text, we choose to plot the deformation free energy ΔF at different reduced Egelstaff-Widom lengths $\varPsi$ on the same scale so as to show how a variation of $\varPsi$ affects the overall magnitude of ΔF, and the range used is adjusted to the $\varPsi = 1$ sets of curves. In turn, the fine details of some of the $\varPsi = 10$ and $\varPsi = 0.1$ curves are not easily visible: For example, the non-convexity of ΔF at $\varPsi = 10$ and $\omega = 1.3$ is obvious in all lattices but that at $\varPsi = 10$ and $\omega = 1.1$ is not although it is there. To show the presence of the distinct features of ΔF that qualitatively affect the phase diagram, we divide the $(\omega, \varPsi)$ parameter space into three regions (Fig. S9). The first one corresponds to drops that are characterized by an attractive interaction at small indentations, which leads to aggregation upon contact; this regime is referred to as *non-monotonic*. The second regime referred to as *non-convex* corresponds to drops with a hump-like deformation free energy where ΔF is convex at small and large indentations but not at intermediate indentations. The third regime referred to as *regular* covers cases where the deformation energy is both monotonic and convex.

The thus defined non-monotonic and the non-convex are not mutually exclusive as illustrated by Fig. S10 which shows ΔF in the BCC lattice at $\varPsi = 10$ and $\omega = 0.9$, which is attractive at small indentations (that is at large specific volumes a little smaller than that where the neighboring drops just touch) and non-convex at intermediate indentations (that is at intermediate specific volumes). Here the non-convexity is due to the attractive interaction between the drop and the next-nearest neighbors. This behavior is generally seen at $\omega < 1$ in all

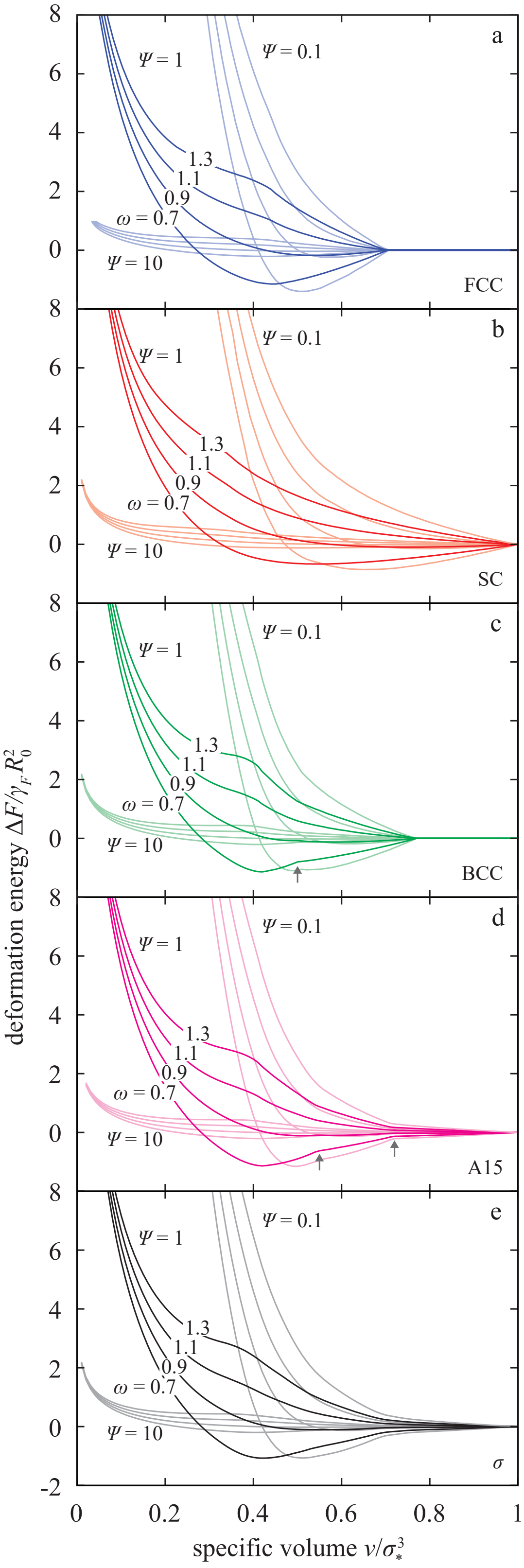

Figure S8: Deformation energy vs. specific volume for FCC, SC, BCC, A15, and σ lattice (a, b, c, d, and e, respectively) for $\varPsi = 0.1, 1,$ and 10 and $\omega = 0.7, 0.9, 1.1,$ and 1.3. Locations of slope discontinuities in the BCC and A15 lattice are indicated by arrows. In the $\varPsi = 0.1$ and the $\varPsi = 10$ sets of curves, labels indicating the value of ω are omitted for clarity; the values and their order is the same as in the $\varPsi = 1$ sets.

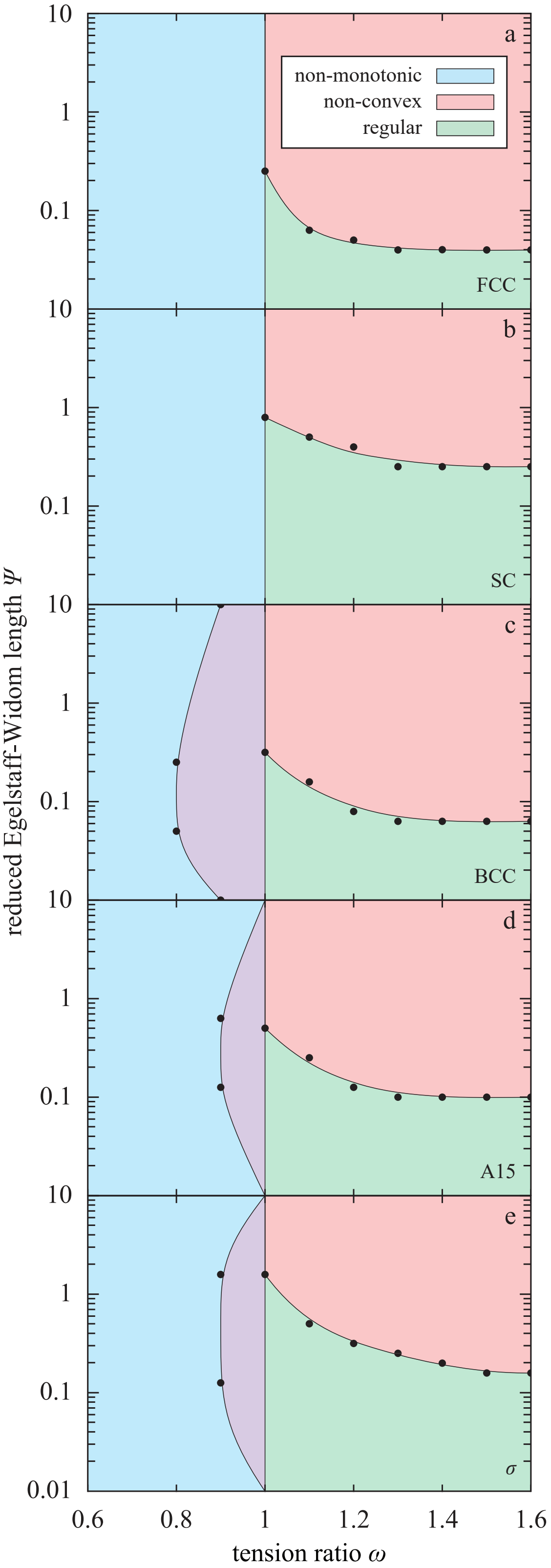

Figure S9: Regions in the (ω, Ψ) plane where the deformation free energy of drops in FCC, SC, BCC, A15, and σ lattice (a, b, c, d, and e, respectively) is non-monotonic (blue) and non-convex (red) function of specific volume; at small Ψ and $\omega > 1$, the free energy is a monotonic and strictly convex function, and this behavior is referred to as regular (green). In the BCC, A15, and σ lattice, the non-monotonic and the non-convex regimes overlap at tension ratios ω somewhat smaller than 1 (magenta). Solid lines are guides to the eye except the vertical boundary of the non-monotonic regime at $\omega = 1$, which is exact.

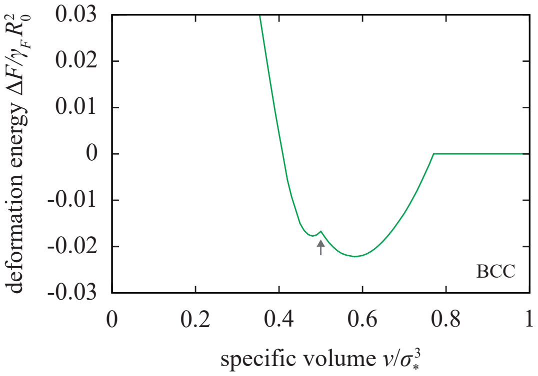

Figure S10: Deformation energy of the BCC lattice at $\Psi = 10$ and $\omega = 0.9$, which is both non-monotonic and non-convex. The vertical arrow indicates the specific volume where the next-nearest neighbors just touch.

lattices where both nearest and next-nearest neighbors are in contact.

In Fig. S9, we show the three regimes for the FCC, SC, BCC, A15, and σ lattice. In all lattices, the $\omega < 1$ domain belongs to the non-monotonic regime. The non-convex regime is located in the $\omega >$ part of the diagram at moderate and large Ψ. In addition, in the BCC, A15, and σ lattice it also occupies a small portion of the $\omega < 1$ part of the diagram where it overlaps with the non-monotonic regime. The $\omega > 1$, small-Ψ part of the diagram belongs to the regular regime. The boundary between the non-convex and the regular regime decreases with ω but saturates at $\omega \gtrsim 1.1$. The precise location of this boundary varies from lattice to lattice.

IV. WET FOAM ANALOGY

A dense suspension of our liquid drops with a packing fraction η smaller than 1 is similar to the wet foam in that a large but not all of the volume is filled by the drops; the voids at the edges and the vertices of the partially faceted drops correspond to the Plateau borders and their junctions (Fig. S11). This analogy is illustrative but incomplete. Firstly, bubbles in foams are usually assumed incompressible so as to reflect the fact that the surface energy of the foam is much smaller than its bulk energy whereas our drops are compressible; in this respect, a wet foam may be regarded as the $\Psi = 0$ limit of the liquid-drop suspension. Secondly, the wet foam is characterized by a single surface tension associated with the gas-liquid interface, which pertains to films that separate neighboring bubbles as well as to Plateau borders and junctions. On the other hand, the description of the liquid-drop suspension requires two surface tensions, one for the drop-drop contact which represents two nanocolloids pushing against each other and one for the solvent-drop contact mimicking the free surface of the colloids.

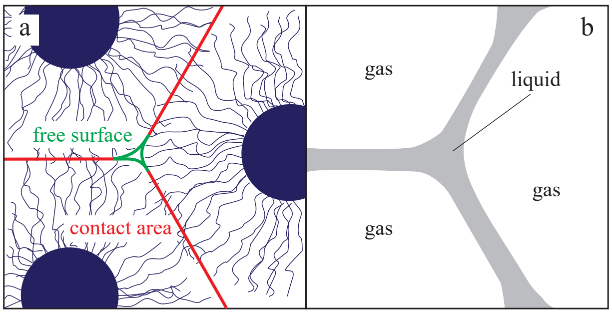

Figure S11: Schematic of closely packed spherical polymer brushes illustrating the difference between the interfacial tension of the drop-drop contact zones and the solvent-drop interfacial tension as two key parameters of the liquid-drop model (a). Panel b shows a cross-section of the wet foam, which is characterized by a single surface tension.

In view of the constant-volume constraint employed in studies of wet foams, it is plausible that the exponent characterizing the small-deformation regime is somewhat larger than our $\omega = 1$ exponent of $p \approx 2.0$ and that it increases with the coordination number z. The values reported in Ref. [2] range between 2.1 ($z = 2$) and 2.6 ($z = 20$). Another consequence of the constraint is a smaller range where the deformation energy is independent of z and is thus pairwise-additive for practical purposes. As seen in Fig. 8 in Ref. [2], this range extends to reduced indentations of $h/R_* \approx 0.01$ rather than about 0.05 like in our model (Fig. 3a of the main text).

V. STRUCTURE OF AGGREGATES AT $\omega < 1$

At $\omega < 1$, the deformation energy of the liquid drop in a lattice is characterized by a minimum because the tension of the contact zones is smaller than the solvent-drop interfacial tension. The depth of the minimum depends on the lattice as well as on Ψ and ω. Apart from the kinetic arguments which go beyond the scope of this paper, the stable aggregate structure corresponds to the lattice with the deepest minimum at given Ψ and ω. Figure S12 shows that at $\Psi = 1$, the drops form an FCC aggregate at $\omega \gtrsim 0.65$ whereas at $\omega \lesssim 0.65$ they form a BCC aggregate; for clarity, we do not plot the other lattices considered but only FCC, BCC, SC, A15, and σ lattice. (These pieces of information are also included in the phase diagram in Fig. S13 where we divide the small-density domain at $\omega < 1$ which belongs to aggregates into regions where the aggregates form an FCC and a BCC lattice.)

Figure S12 also shows that the specific volume of the stable aggregate increases with ω and that the aggregates are more strongly bound at small ω as expected. The dependence of the binding energy on the reduced Egelstaff-Widom length Ψ and on the tension ratio ω will be studied in detail in a forthcoming publication.

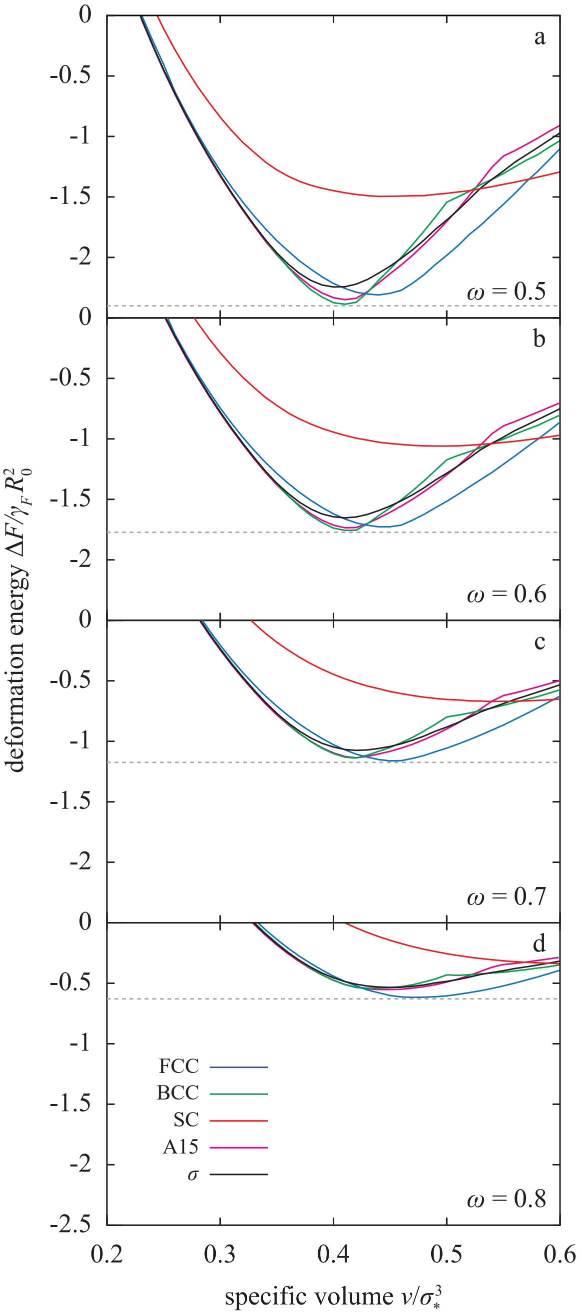

Figure S12: Deformation energies of the lowest-lying lattices vs. specific volume for $\Psi = 1$ and $\omega = 0.5 - 0.8$ (top to bottom). For $\omega \lesssim 0.65$, the minimum corresponds to the BCC lattice whereas for ω between 0.65 and 1 it corresponds to the FCC lattice. The dashed line shows the binding energy.

VI. PHASE DIAGRAM

Figure S13 shows the phase diagram at tension ratio ω between 0.6 and 1.3, complementing Fig. 5 of the main text with a finer level of detail. At $\omega > 1.3$, the phase diagram does not change very much qualitatively, the only new phase being the oblate simple hexagonal (SH) lattice at $\omega \gtrsim 1.5$ as discussed below.

The $\omega = 1$ results may be compared to the $T = 0$ phase diagram of particles interacting with a harmonic pair repulsion [3]. In the range of reduced densities up to $\rho\sigma_*^3 = 4$ covered in Fig. 5 of the main text, the phase sequence of these particles is fluid-FCC-BCC-base-centered orthorhombic (baco)-SH [3] where the ratios of lattice parameters in the baco lattice are $b/a = 1$ and $c/a = 0.73$ whereas in the SH lattice it is $c/a = 0.61$. This sequence is quite distinct

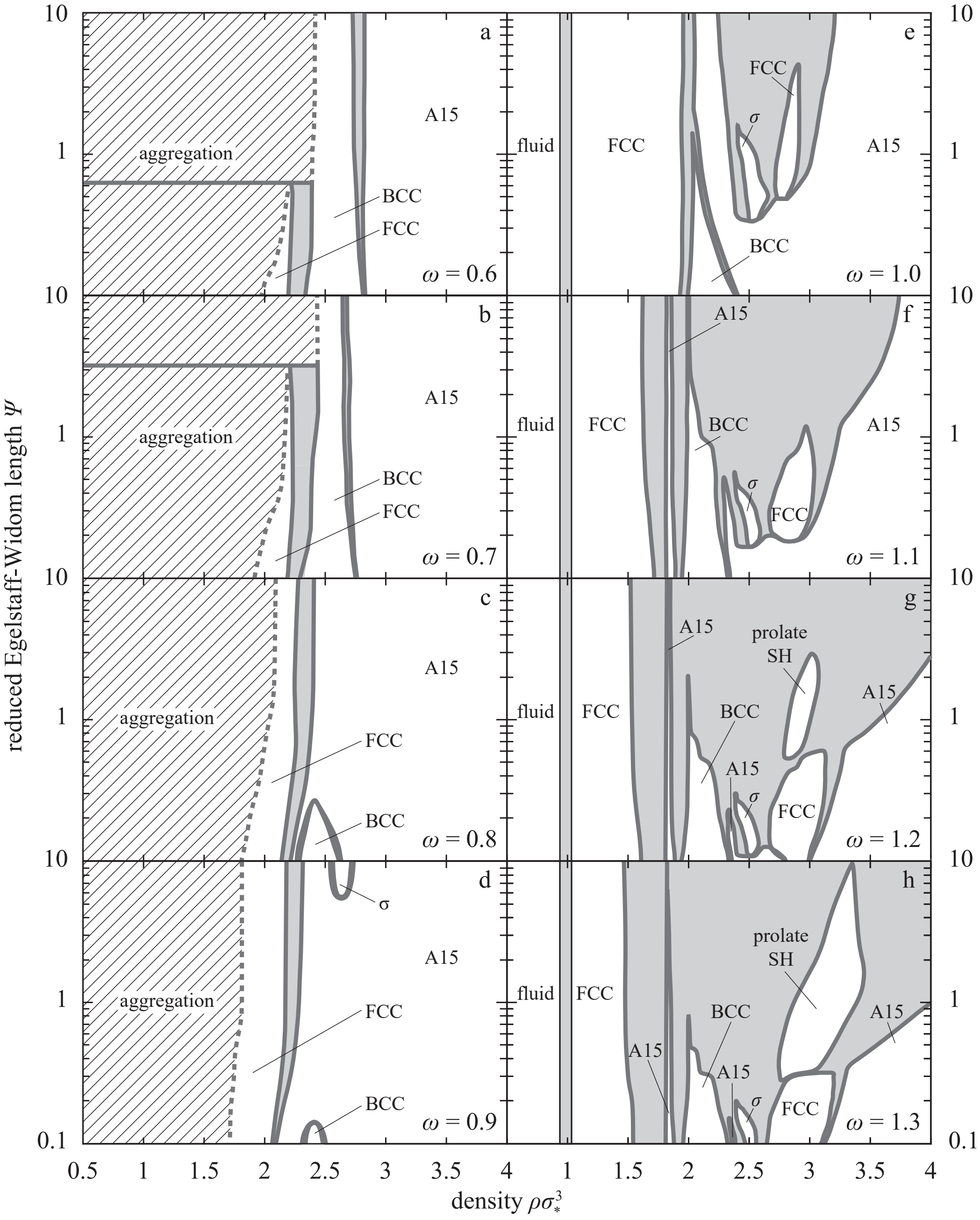

Figure S13: Phase diagram in the $(\rho\sigma_*^3, \Psi)$ plane for $\omega = 0.6, 0.7, \ldots 1$ (panels a, b, ... h, respectively). Phase boundaries are drawn using thick lines so as to indicate the estimated numerical inaccuracy. In panels a–d, the dashed line indicates the density of the stable aggregate; at densities smaller than this aggregates are in coexistence with vacuum.

from our phase diagram at any Ψ, one of the main differences being the absence of the A15 crystal in Ref. [3]: This phase was considered as a trial lattice but found not to be stable. In addition, the coexistence regions of the harmonic pair repulsion model are rather narrow whereas they are broad in the liquid-drop model (Fig. S13). This comparison shows that the many-body effects at work in the liquid-drop model are very prominent if not essential.

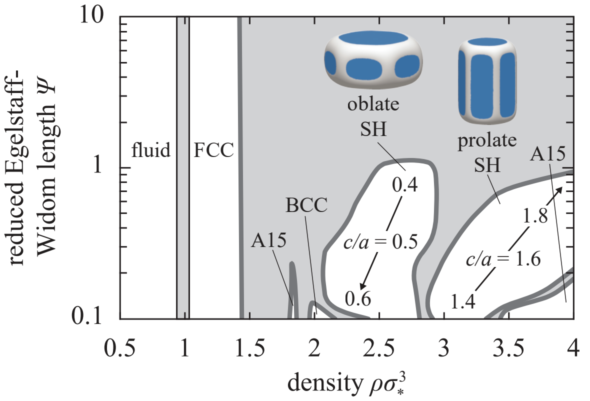

Figure S14: Phase diagram at $\omega = 2$ featuring the oblate and the prolate SH lattice. Labels in the SH regions indicate the ratio of lattice parameters c/a in a specific part of the region; naturally, c/a varies in a continuously across the regions. Also shown are two representative snapshots of the drop from the oblate and the prolate domain, the former at $\Psi = 0.5, \rho\sigma_*^3 = 2.5$, and $c/a = 0.5$ and the latter at $\Psi = 0.5, \rho\sigma_*^3 = 3.3$, and $c/a = 1.5$.

At tension ratio $\omega \gtrsim 1.3$, the SH lattice is rather prominent. The prolate branch with $c/a > 1$ appears in the phase diagram at $\omega \approx 1.2$ and as ω is increased, it occupies an increasingly larger region centered roughly at $\rho\sigma_*^3 \approx 3$. The ratio of lattice parameters in the prolate region ranges from about 1.4 to about 2.0, the bounds depending on ω. Beyond $\omega \approx 1.5$, the oblate SH branch with $c/a < 1$ is also present at somewhat smaller densities, and the domain of stability of the oblate region increases with ω. Figure S14 shows the phase diagram at $\omega = 2$ where both branches of the SH phase are rather large and located at $\Psi < 1$.

The stability of the SH lattice at intermediate densities can be understood by examining its deformation energy. Figure S15 shows the deformation energy as a function of specific volume, and we see that the energies of both oblate and prolate branch are marked by a knee associated with a change of coordination number. For clarity, we plot the deformation energy of two representative SH lattices with $c/a = 0.5$ and 1.5. In the former, the coordination number increases from 2 to 8 at $v/\sigma_*^3 \approx 0.43$, which leads to a dramatic change of slope. In the prolate branch, this effect is less prominent but it still gives rise to a knee-like profile of the deformation energy. As the knees of both curves are located in the middle of the non-convex sections of the deformation energies of the other trial lattices (in Fig. S15 we only show the energies of FCC, BCC, and A15 lattice for clarity) the SH lattice with a suitable ratio of lattice parameters c/a is stable.

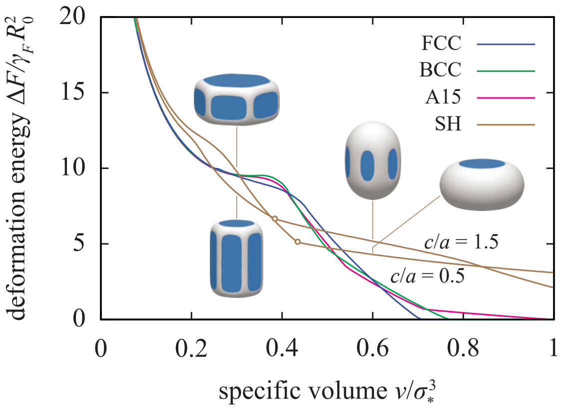

Figure S15: Deformation energy vs. specific volume for drops with $\omega = 2$ in FCC, BCC, and A15 as well as SH lattice with $c/a = 0.5$ and 1.5. The knees in the SH curves at $v/\sigma_*^3 = 0.43$ and 0.38, respectively, are marked with open circles. Insets show the shape of the liquid drop in the oblate and the prolate SH branch at large specific volumes where the drops are in contact with 2 and 6 neighbors, respectively, and at small specific volumes where they push on all 8 neighbors.

It is not too difficult to imagine that if the ratio c/a is varied, the knees in the deformation energies in both variants of the SH lattice are shifted, and thus the phase diagram includes an oblate and a prolate SH region with c/a continuously varying from point to point.

The $(\rho\sigma_*^3, \Psi)$ representation of the phase diagram is convenient for comparison with experiments where the only quantity varied is density. This is not always the case; often temperature is varied instead. Among the three material parameters needed to describe drops in contact—the solvent-drop interfacial tension γ_F, the drop-drop contact tension γ_C, and the drop compressibility χ_T—, γ_C and χ_T can used to independently control the tension ratio ω and the reduced Egelstaff-Widom length Ψ. On the other hand, the solvent-drop interfacial tension γ_F (which depends on solvent quality) appears in both ω and Ψ. An decrease of γ_F at fixed γ_C and χ_T thus leads to an increase of ω and a simultaneous decrease of Ψ. In this case, neither the $(\rho\sigma_*^3, \Psi)$ nor the $(\rho\sigma_*^3, \omega)$ representation of the phase diagram are the most telling ones.

VII. DROP VOLUME VS. SPECIFIC VOLUME

The secondary horizontal axis in Fig. 6 of the main text is linear in the complete-faceting regime and increasingly more non-linear in the partial-faceting regime as drop volume approaches the resting volume where the drops just touch. This relationship is more clearly represented

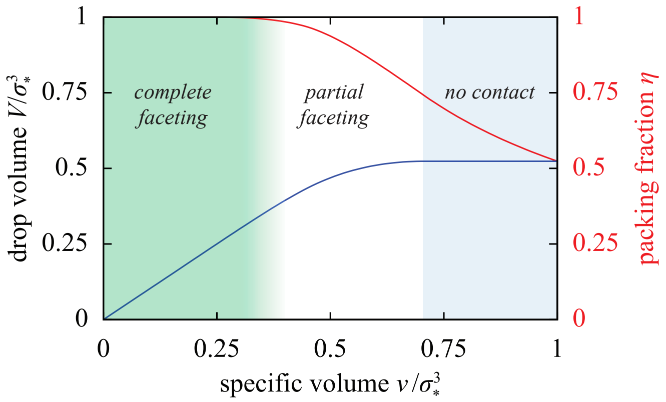

Figure S16: Volume of drop in FCC lattice plotted against specific volume for $\Psi = 1$ and $\omega = 1$; also included is the packing fraction. The drops are in contact at specific volumes smaller than ≈ 0.707.

in Fig. S16 where we plot the volume of drops in FCC lattice together with the packing fraction as a function of the specific volume for $\Psi = 1$ and $\omega = 1$. The drops are in contact at specific volumes $v < 0.707$ and Fig. S16 shows that down to $v \approx 0.6$ the drop volume hardly decreases. On the other hand, from $v \approx 0.4$ down to 0 where the packing fraction is almost 1, the drop volume is essentially the same as the specific volume.

The dependence of drop volume on the specific volume at $\Psi = 1$ and $\omega = 1$ shown in Fig. S16 is representative of all values of the reduced Egelstaff-Widom length Ψ and tension ratio ω, the variation of $V(v)$ with Ψ and ω being as limited as the variation of packing fraction η shown in Fig. 2c of the main text.

VIII. ON PHYSICAL MEANING OF REDUCED EGELSTAFF-WIDOM LENGTH Ψ

Here we resort to statistical mechanics of polymers to estimate the physically relevant ranges of the reduced Egelstaff-Widom length Ψ by relating it to the osmotic equation of state for macromolecules. As a preliminary note, we emphasize that the surface tension of the liquid-drop model γ_F is an effective parameter describing the nanocolloidal particle as a whole and it should not be confused with the polymer-solvent surface tension. Indeed, as demonstrated by explicit calculations [4], the real surface tension between a (grafted) polymer and a good solvent is negative because a good solvent does enter into the brush. Instead, our positive γ_F is representative of the forces within a polymer brush which hold the brush together, due to the connectivity of the monomers and the grafting of the chains onto the central colloidal core: Without it, the individual monomers would disperse. In the liquid-drop model the monomers are indeed viewed as disconnected albeit held together by the van der Waals attractive forces included in the Murnaghan equation of state [which corresponds to the first term in Eq. (1) of the main text], and a positive surface tension γ_F represents the effect of chain connectivity as the main cohesive force in the brush.

We now relate the effective surface tension γ_F and χ_T as the material model parameters to the osmotic equation of state, seeking scaling-theory arguments for the dependence of Ψ on the monomer density within the nanocolloid. The surface tension is related to the osmotic pressure Π via the Laplace law

$$\frac{2\gamma_F}{R_*} = \Pi, \tag{S14}$$

where R_* is the resting radius of the drop. Let us now consider a soft polymeric nanocolloid such as a brush, a cross-linked microgel, a dendritic brush, or a randomly branched polymer. We assume that there are N monomers within the colloid so that the monomer density reads

$$\phi = \frac{N}{V_*}, \tag{S15}$$

where $V_* = 4\pi R_*^3/3$ is the resting volume of the colloid. The reduced Egelstaff-Widom length [Eq. (2) of the main text] can be cast as

$$\Psi = \lambda_\Psi \frac{2\gamma_F}{R_*}\chi_T, \tag{S16}$$

where $\lambda_\Psi = R_*/R_0$ is the ratio of the resting and the reference radii of the drop [1] representing the shrinkage of the drop due to surface tension. Together with Eq. (S14), Eq. (S16) states that Ψ scales as

$$\Psi \cong \Pi\chi_T. \tag{S17}$$

The value of the isothermal compressibility χ_T pertains to the reference state of the model where the surface tension vanishes, whereas the physically relevant value in the resting state at a finite tension [and thus a finite osmotic pressure; see Eq. (S14)] differs from it by a numerical factor of $V_*/V_0 = \lambda_\Psi^3$. Within the scope of the scaling theory, we can thus estimate χ_T by

$$-\frac{1}{V_*}\left(\frac{\partial V_*}{\partial \Pi}\right)_T \tag{S18}$$

and since $\partial/\partial V_* = -(N/V_*^2)\partial/\partial\phi$, we find that

$$\chi_T \cong \frac{1}{\phi\Pi'(\phi)}. \tag{S19}$$

From Eqs. (S17) and (S19) we finally obtain

$$\Psi \cong \frac{\Pi(\phi)}{\phi\Pi'(\phi)} \tag{S20}$$

Equation (S20) relates the monomer density ϕ within the nanocolloidal particle with the value of Ψ via the osmotic equation of state $\Pi(\phi)$ of the polymer that constitutes the particle. Here we assume that the polymer within the particle can be treated as bulk material and view it as a polymer solution.

Let us now examine a few special cases.

A. Dilute polymer brushes

In the dilute limit, that is for ϕ smaller than the overlap density ϕ_*, the osmotic pressure is given by the van't Hoff law [5] and proportional to the monomer density

$$\Pi \propto \phi \tag{S21}$$

so that

$$\Psi \sim 1 \tag{S22}$$

independent of monomer density ϕ.

B. Semidilute polymer brushes

Semidilute polymer brushes are self-similar. As a consequence, their equations of state are power-law functions of ϕ [5], namely

$$\Pi(\phi) = C\phi^{\mu}. \tag{S23}$$

Here C is a constant of the form $k_BT\ell^{3(\mu-1)}$, ℓ being some length scale which could involve, e.g., the excluded volume v_0 or the three-body term w for the Θ solutions as well as the bond size b. The precise value of ℓ is however irrelevant because from Eqs. (S20) and (S23) we obtain

$$\Psi \sim \frac{1}{\mu}, \tag{S24}$$

again independent of monomer density ϕ. For good solvents, results from Ref. [1] fully confirm the validity of Eq. (S24): In this reference Ψ was found to be ≈ 0.6 independent of the functionality f and the number of monomers N; i.e., independent of ϕ. Specifically, $\Pi(\phi) \sim \phi^3$ in Θ solvents whereas $\Pi(\phi) \sim \phi^{9/4}$ in good solvents [5]. Since $\mu_\Theta > \mu_{\text{good solvent}}$, we can expect that $\Psi_\Theta < \Psi_{\text{good solvent}}$ based on Eq. (S24).

On going from the dilute to the semidilute regime, the reduced Egelstaff-Widom length Ψ should thus decrease from a value or order 1 to a smaller value, which is larger in good solvents than in poor solvents (Fig. S17). In star polymers and in spherical polymer brushes, the simplest way of changing ϕ is by changing the functionality and the grafting density, respectively. Quite generally, we conclude that in the dilute and in the semidilute regime Ψ decreases with chain number and increases as solvent quality is improved.

C. Crowding-dominated regime

Figure S17 also covers the behavior of Ψ in the crowding-dominated regime at large ϕ. Here the osmotic pressure $\Pi(\phi)$ increases more steeply with ϕ than in the semidilute regime. Indeed, as the density of the polymer solution crosses over from the semidilute regime to the melt, details of the monomer-monomer interactions start playing a role, leading to non-universal equations of state and to a steep increase of the pressure, which reflect the increasingly relevant crowding of individual, repulsive monomers. Accordingly, the equation of state attains a generic form similar to the one sketched in Fig. S18 (see, e.g., Fig. 1 in Ref. [6]).

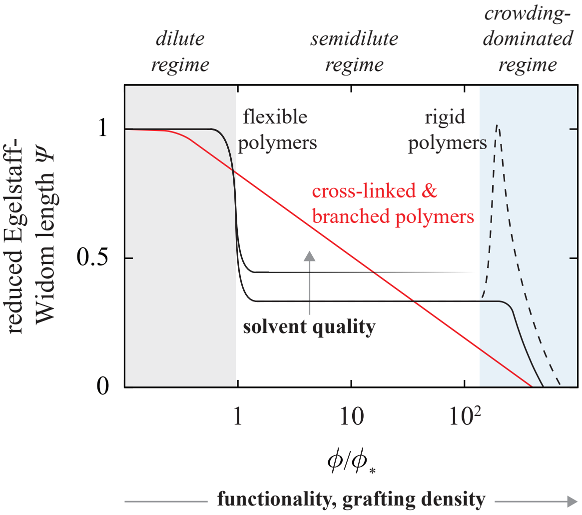

Figure S17: Dependence of Ψ on monomer density within the nanocolloidal particle with the solvent-controlled plateau in brushes in the semidilute regime, the generally decreasing trend characteristic of branched and cross-linked polymers, and anomalous increase in rigid polymers at high densities.

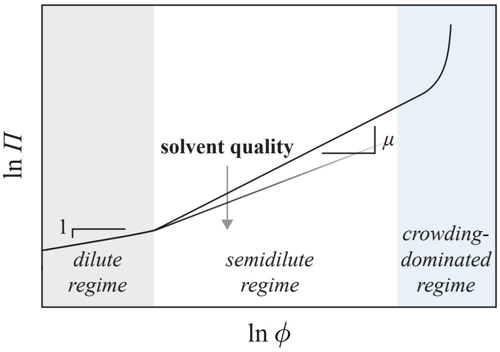

Figure S18: Schematic log-log plot of the osmotic pressure in a flexible-chain polymer brush in the dilute, semidilute, and crowding-dominated regime.

In the crowding-dominated regime, the reduced Egelstaff-Widom length depends on ϕ. This is easily seen by rewriting Eq. (S20) as

$$\Psi \sim \left[\frac{\mathrm{d}\ln\Pi(\phi)}{\mathrm{d}\ln\phi}\right]^{-1}. \tag{S25}$$

The log-log plot of $\Pi(\phi)$ in Fig. S18 readily shows that at any density ϕ in the crowding-dominated regime the derivative $\mathrm{d}\ln \Pi(\phi)/\mathrm{d}\ln\phi$ is larger than in the semidilute regime and thus Ψ in the crowding-dominated regime is smaller than the semidilute-regime value of $1/\mu$. This argument explains the decrease of Ψ at high densities shown in Fig. S17.

An explicit illustration of this behavior may start from a model equation of state of type $\Pi(\phi) \propto (\phi_0 - \phi)^{-m}$ where $m > 0$ and $\phi < \phi_0$. This model describes a diverging pressure as the "jamming limit" $\phi \to \phi_0^-$ is approached, which qualitatively agrees with Fig. S18. This immediately gives

$$\Psi \propto \frac{\phi_0 - \phi}{m\phi} \tag{S26}$$

which goes to 0 as $\phi \to \phi_0$. We conclude that the reduced Egelstaff-Widom length Ψ further decreases in the crowding-dominated regime, and this should allow one to experimentally explore the most interesting part of the phase diagram in Fig. 5 of the main text and Fig. S13, which is at small Ψ.

D. Branched and cross-linked polymers

These ideas can be transplanted to branched and cross-linked polymers. For example, Fig. 10 in Ref. [7] shows that dendrimers are characterized by an equation of state that qualitatively looks like that in Fig. S18. Based on this finding, we can expect that in dendrimers and other regularly or randomly branched polymers too Ψ should decrease with ϕ, except that in these systems the decrease should be gradual rather than step-like as they are not self-similar. In these systems, we can effectively crowd the brush with monomers at will by changing dendritic generation and/or branching number [8].

E. Rigid-chain brushes

In semiflexible and rigid chains, the osmotic pressure is characterized by a cusp at intermediate monomer densities as seen in Fig. 10 in Ref. [9] (schematically shown in Fig. S19). This feature is associated with a (partial) nematic orientational order of the chains induced by compression. Beyond the cusp, the osmotic pressure increases with ϕ more slowly than below the cusp, although at higher densities still its slope again becomes larger. As a result Ψ should here increase with ϕ beyond the cusp, and then it should decrease again at high enough ϕ as shown with the dashed line in Fig. S17. This non-monotonic behavior of the reduced Egelstaff-Widom length Ψ is more challenging from the experimental perspective but nonetheless possible, say in polyelectrolyte or DNA chains.

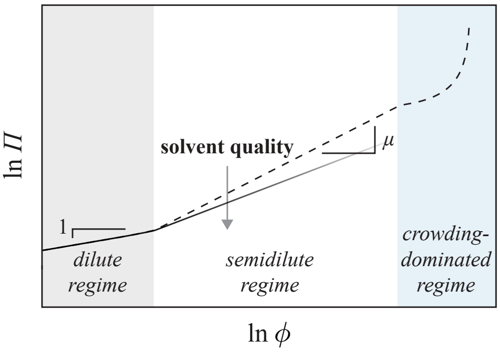

Figure S19: Schematic log-log plot of the osmotic pressure in a rigid-chain polymer brush in the dilute, semidilute, and crowding-dominated regime.

F. Scanning phase diagram

In conclusion, these arguments suggest that the theoretical phase diagram of the liquid-drop model can be experimentally explored by changing solvent quality, brush functionality, chain branching or cross-linking, and chain rigidity. This is schematically summarized in Fig. S20 where we redraw the $\omega = 1.1$ phase diagram [Fig. 5c of the main text and Fig. S13f] with overlaid trajectories corresponding to spherical linear-chain brushes in good and poor solvents and at small and large functionalities. These trajectories represent a cut across the phase diagram obtained, e.g., upon compression or expansion. In turn, solvent quality can be controlled by changing tem-

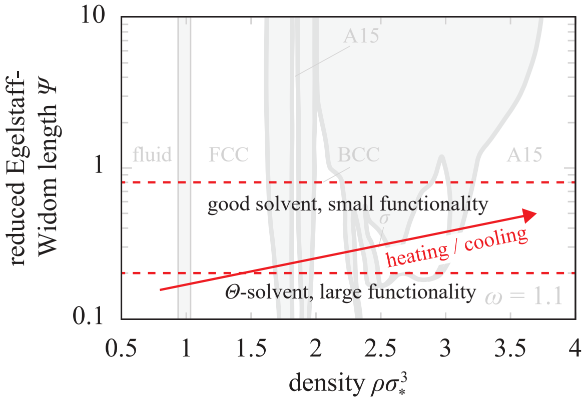

Figure S 20: Phase diagram of the liquid-drop model in the $(\rho\sigma_*^3, \Psi)$ at $\omega = 1.1$ with schematically indicated sequences that should be experimentally achievable with spherical linear-chain brushes upon increasing density in good and Θ-solvents and at small and large functionalities. Also included is a schematic trajectory expected upon heating or cooling at fixed density of the spherical-polymer-brush particles for the normal case, in which the solvent quality improves with temperature.

perature or pH, and these two parameters indeed appear to be the simplest quantities to vary so as to change Ψ in a given sample.

In case the phase diagram were scanned by changing temperature rather than density, one should expect to observe a phase sequence corresponding to a diagonal rather than a horizontal trajectory across Fig. S20 because an increase of temperature will, for the vast majority of solvents and polymers, i) improve solvent quality, which will in turn ii) increase the diameter of, e.g., a star-polymer nanocolloidal particle [10] and hence the reduced density. A schematic cut across the phase diagram expected in a heating/cooling run is also shown in Fig. S20.

IX. ON PHYSICAL MEANING OF TENSION RATIO ω

To determine the realistic range of the ratio of effective interfacial tension of the contact zones and (twice) the effective tension of the solvent-drop interface

$$\omega = \frac{\gamma_C}{2\gamma_F}, \tag{S27}$$

we employ scaling and other theoretical arguments. As per the tension of the solvent-drop interface γ_F, in Ref. [1] it was shown that it scales as

$$\gamma_F = k_B T \frac{f^{3/2}}{R_*^2}, \tag{S28}$$

where f is the functionality of the spherical polymer brush or star polymer. The interfacial tension of the contact zones γ_C which measures the free energy per unit area when two brushes come in contact can be estimated by resorting to the interaction potential [11] between two star polymers, which is repulsive and reads

$$u(r) = \frac{5}{18} k_B T f^{3/2} \begin{cases} -\ln\left(\frac{r}{2R_*}\right) + \frac{1}{1+\sqrt{f}/2}, & r \le 2R_* \\ \frac{1}{1+\sqrt{f}/2}\frac{2R_*}{r}\exp\left(-\frac{\sqrt{f}}{2}\frac{r-2R_*}{2R_*}\right), & r > 2R_* \end{cases}. \tag{S29}$$

We consider two such stars when they first come in contact as their center-to-center distance is decreased from a large value. If we model them as spheres of radius R_*, they touch at $r = 2R_*$ (Fig. S21).

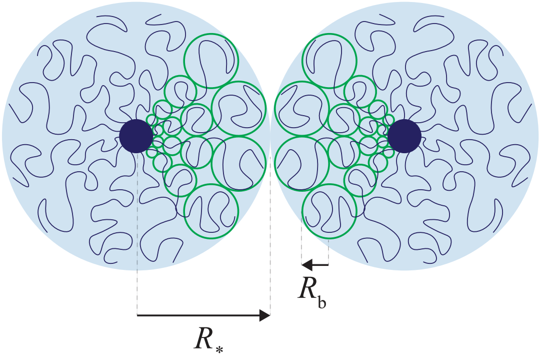

Figure S 21: Two star polymers in contact, showing the Daoud-Cotton blobs along some of the arms.

According to Eq. (S29), the free energy penalty for touching is

$$u(r = 2R_*) = \frac{5}{18}\frac{k_B T f^{3/2}}{1+\sqrt{f}/2} = \frac{5}{9} k_B T \sqrt{f}, \tag{S30}$$

the last result applying to the limit of large f. The radius of the outermost Daoud-Cotton blob R_b (see Ref. [11] and Fig. S21) is estimated by realizing that the surface of the star polymer consists of f discs of radius R_b. Thus $f R_b^2 = R_*^2$ and

$$R_b = \frac{R_*}{\sqrt{f}}. \tag{S31}$$

Since the surface area of the contact of two stars when they just touch is of the order of R_b^2, we obtain from Eqs. (S30) and (S31)

$$\gamma_C \sim \frac{u(r = 2R_*)}{R_b^2} \sim \frac{k_B T \sqrt{f}}{(R_b/\sqrt{f})^2} = k_B T \frac{f^{3/2}}{R_*^2}. \tag{S32}$$

There is a remarkable coincidence between Eqs. (S28) and (S32): Both γ_F and γ_C scale the same way with all three relevant parameters, $k_B T$, f, and R_*. Although the scaling $\sim k_B T/R_*^2$ is expected on dimensional grounds, the common $f^{3/2}$ term is nontrivial, having its physical origin in the number of blobs in the brush. Thus we conclude that the tension ratio ω is generally of order 1:

$$\omega \sim 1. \tag{S33}$$

This is an important result because it implies that by varying the parameters that affect the precise value of the two tensions, we can make ω either smaller or larger than unity and thus explore both the $\omega < 1$ regime characterized by attractive drops and aggregation at small densities as well as the $\omega > 1$ regime characterized by repulsive drops and a stable fluid phase at small densities (Fig. S13).

Experimental results are consistent with $\omega > 1$ simply because in homopolymer-based star polymers and in spherical polymer brushes, aggregation has not been observed. On the other hand, spontaneous aggregation behavior seen in numerous studies of end-functionalized star polymers and brushes (see, e.g., Refs. [12–14]) can also be viewed as a manifestation of $\omega < 1$ in these cases. Indeed, it is plausible that modification or functionalization of endgroups will affect γ_C but not γ_F; the latter scales as $\sim \mathit{\Pi} R_*$ and is determined by the behavior of the bulk of star polymers whereas the former can be either increased (by big endgroups, charge, etc.) or decreased (by attractive or zwitterionic endgroups).

In conclusion, we showed that for polymer brushes in good solvents the tension ratio $\omega \gtrsim 1$ but can be either increased or decreased by a suitable choice of endgroups. In turn, this implies that for different nanocolloids the value of ω is less universal than is the reduced Egelstaff-Widom length $\mathit{\Psi}$.

[1] J. Riest, L. Athanasopoulou, S. A. Egorov, C. N. Likos, and P. Ziherl, Sci. Rep. **5**, 15854 (2015).

[2] M.-D. Lacasse, G. S. Grest, and D. Levine, Phys. Rev. E **54**, 5436 (1996).

[3] Y.-L. Zhu and Z.-Y. Lu, J. Chem. Phys. **134**, 044903 (2011).

[4] D. I. Dimitrov, A. Milchev, and K. Binder, J. Chem. Phys. **127**, 084905 (2007).

[5] M. Rubinstein and R. H. Colby, *Polymer Physics* (Oxford University Press, Oxford, 2003).

[6] A. Milchev, J. P. Wittmer, P. van der Schoot, and D. Landau, Europhys. Lett. **54**, 58 (2001).

[7] L. Lue and M. Prausnitz, Macromolecules **30**, 6650 (1997).

[8] O. V. Rud, A. A. Polotsky, T. Gillich, O. V. Borisov, F. A. M. Leermakers, M. Textor, and T. M. Birshtein, Macromolecules **46**, 4651 (2013).

[9] V. A. Ivanov, E. A. An, L. A. Spirin, M. R. Stukan, M. Müller, W. Paul and K. Binder, Phys. Rev. E **76**, 026702 (2007).

[10] C. N. Likos, Phys. Rep. **348**, 267 (2001).

[11] C. N. Likos. H. Löwen, M. Watzlawek, B. Abbas, O. Jucknischke, J. Allgaier, and D. Richter, Phys. Rev. Lett. **80**, 4450 (1998).

[12] F. Lo Verso, A. Z. Panagiotopoulos, and C. N. Likos, Faraday Discuss. **144**, 143 (2010).

[13] C. Koch, A. Z. Panagiotopoulos, F. Lo Verso, and C. N. Likos, Soft Matter **9**, 7424 (2013).

[14] R. A. Brady, N. J. Brooks, P. Cicuta, and L. Di Michele, Nano Lett. **17**, 3276 (2017).